



Enhanced Photocatalytic Performance of Al-Doped ZnO NPs-Reduced Graphene Oxide Nanocomposite for Removing of Methyl Orange Dye from Water Under Visible-Light Irradiation

S. Asghar Khayatian¹ · Ahmad Kompany² · Nasser Shahtahmassebi² · A. Khorsand Zak³

Received: 24 May 2018 / Accepted: 30 July 2018
© Springer Science+Business Media, LLC, part of Springer Nature 2018

Abstract

In this work, a series of Al-doped ZnO nanoparticles-reduced graphene oxide (AZO–RGO) nanocomposites were successfully synthesized by loading AZO nanoparticles (AZO NPs) on the graphene oxide sheets via in situ and low temperature solvothermal method. Several techniques were utilized to characterize the resultant nanocomposites including scanning electron microscopy (SEM), transmission electron microscopy (TEM), X-ray diffraction (XRD), atomic force microscopy, X-ray photoelectron spectroscopy (XPS), and FT-Infra Red (FT-IR) analyses. SEM and TEM studies showed that AZO NPs have been formed on RGO surface, confirming the formation of AZO–RGO nanocomposites. XPS, FT-IR, and XRD analyses revealed that the oxygen-containing functional groups can prepare as anchoring sites for capturing AZO NPs on RGO surface. Moreover, it was observed that these nanoparticles have wurtzite structure. The photo-catalysis results showed that the 5% AZO–RGO nanocomposite has a higher efficiency than that of pure ZnO and ZnO–RGO samples for removing methyl orange dye from water under visible light irradiation. The enhancement in the photocatalytic activity can be attributed to the increase of surface area of AZO–RGO nanocomposites in comparison with pure ZnO. Furthermore, the existing of Al dopants and RGO sheets in the prepared samples can effectively decrease the charge recombination process in the AZO–RGO nanocomposites.

Keywords ZnO · AZO nanoparticle · Graphene oxide sheet · Nanocomposite · Photocatalytic activity

1 Introduction

Nowadays, organic dyes and pigments in the aquatic ecosystems are considered among the greatest environmental threats due to their high solubility feature. According to the published reports, considerable amounts of dyes (~5–15%) used in many industries, easily penetrate into the environment [4, 6]. In recent years, several techniques have been employed to eliminate and destroy these organic pollutants such as adsorption

[14, 40], advanced oxidation procedures [52] and chemical oxidation routes [45]. During the last decade, the metal oxide semiconductors have been widely used to remove the harmful organic dyes from water based on the photocatalytic degradation. These materials have some important advantages including simplicity, low energy need and disintegration of organic pollutants into the less dangerous components. Accordingly, among different metal oxide semiconductors, the nanostructured semiconductors with the energy band gap of 1–4 eV have shown the highest degradation efficiency [5]. Therefore, the semiconductors such as TiO₂, ZnO, WO₃ and CuO have been subjected to intense research as a photocatalytic materials [11, 55]. ZnO and TiO₂ nanostructures have widely attracted the attention of many researchers among different semiconductor photo-catalysts because of their low cost, abundance, physical and chemical stability and nontoxicity [67]. Although, ZnO is one of the most favorable photo-catalysts, its photocatalytic activity is limited to its wide energy band gap (about 3.3 eV at room temperature) [1]. This wide energy band gap can effectively increase the photo-generated electron–hole pair

✉ S. Asghar Khayatian
s.a.khayatian@qiau.ac.ir

¹ Department of Physics, Qazvin Branch, Islamic Azad University, Qazvin, Iran

² Materials and Electroceramics Laboratory, Department of Physics, Faculty of Science, Ferdowsi University of Mashhad, Mashhad, Iran

³ Nanotechnology Laboratory, Esfarayen University of Technology, Esfarayen, North Khorasan, Iran

recombination in ZnO, resulting in a decrease in photocatalytic activity. A well-known operative technique for improving the photocatalytic activity of ZnO is the creation of retarding in the recombination process. Hence, many efforts have been performed by researchers to prevent the electron–hole pair recombination in ZnO-based catalysts. It can be divided into two major sections: (i) doping of ZnO with metals, transition metals and nonmetals [31, 68] and (ii) hybridization of ZnO with other semiconductors and carbonaceous materials (such as activated carbon, carbon nanomaterials, graphene oxide, and graphene) [30, 32, 48, 49]. To improve the photocatalytic activity of ZnO NPs, many transition metals such as Co [61], Pd [69], Mn [60], Ag [13], Sm [43], and Al [1] have been used as dopants. Among these nanoparticles, Al-doped ZnO nanostructures have received considerable attention because of having low-cost raw materials and their unique physio-chemical properties. Besides, various carbonaceous materials such as graphene oxide and graphene are used to develop the photocatalytic efficiency of ZnO structures. These materials have the sheet-like structure to stick nanostructured semiconductors on their basal plane, resulting in the suppression of the photo-induced electron–hole pair recombination. Therefore, a wide range of graphene-based photocatalytic composites including graphene (GR)-TiO₂, GR-ZnO, and GR-WO₃ has been studied [9, 16, 58]. Zhang et al. [67] synthesized Pd-decorated ZnO-graphene oxide (GO) composite for improving its photocatalytic performance on methylene blue. They observed that the composite exhibits higher photocatalytic efficiency than pure ZnO by increasing of the ratio of ZnO–GO. Similar enhancement was also reported by Zeng et al. [65] in Au–ZnO nanocrystals-graphene hybrid, attributing to the decrease of the recombination process. Numerous studies have also been done to enhance the photocatalytic activity of the semiconductors using graphene oxide. All of these attempts confirmed that the decoration of graphene oxide by semiconductor nanoparticles (NPs) could enhance the photocatalytic efficiency [19, 59]. To the best of our knowledge, there is no report on the synthesis and photocatalytic activity of Al doped ZnO NPs-reduced graphene oxide (AZO–RGO) nanocomposites. In this work, we have first synthesized AZO–RGO nanocomposites by a facile solvothermal method and then investigated the photocatalytic property of the samples for removing methyl orange dye from water solution under visible light irradiation.

2 Experimental Details

2.1 Preparation of Photo-catalyst

Natural graphite (99.9%, Alfa Aesar) was used to synthesize graphene oxide (GO) sheets via a modified Hummer's method [21]. To obtain AZO–RGO nanocomposites through a solvothermal route with different Al concentrations, three

different solutions were prepared as follows: (i) 10 wt% of GO was sonicated in 80 ml ethylene glycol (EG) for 1 h to achieve a homogenous brown suspension (Solution 1), (ii) 80 ml of zinc nitrate hexahydrate (Zn(NO₃)₂·6H₂O, 98%) was dissolved in 80 ml EG and then a certain amount of aluminum nitrate nine hydrate was added into it by stirring (Solution 2) and (iii) 20 ml of NaOH was also dissolved into 20 ml deionized water (DI) (Solution 3). In the next step, Solutions 2 and 3 were simultaneously added to the Solution 1 and stirred for another 1 h. In the following, the prepared mixing solution was transferred into a 200 ml Teflon-lined stainless steel autoclave and kept at 160 °C for 24 h. After this time, the final solution was naturally cooled down to room temperature and then centrifuged to acquire the nanocomposite. Consequently, the resultant product was rinsed with ethanol and DI water for several times and fully dried in an oven at 80 °C for 24 h. The amount of aluminum nitrate nine hydrate in the as-prepared AZO–RGO nanocomposites was controlled to be 1, 3, and 5 wt% and the corresponding nanocomposites were labeled as 1% AZO–RGO, 3% AZO–RGO, and 5% AZO–RGO, respectively.

2.2 Characterization

The surface morphology of GO sheet and AZO–RGO nanocomposite was investigated by scanning electron microscopy (SEM, Leo-1450VP, Germany). Moreover, an atomic force microscopy (AFM, Ara Research, Full plus, Iran) with non-contact mode, was also used to evaluate the roughness of graphene oxide sheet. Transmission electron microscopy (TEM, Leo-912AB, Germany) and energy-dispersive X-ray (EDX) analyses were applied to study the distribution of AZO NPs on RGO sheet and the chemical composition of the as-prepared samples. Brunauer–Emmett–Teller (BET) technique was used to measure the specific surface area of the synthesized nanocomposites with the nitrogen adsorption isotherms apparatus (PHS 1020, China). In addition, the crystalline structure of GO, pure ZnO and AZO–RGO samples was studied by X-ray diffractometer (XRD, Unisantis XMD300) with Cu K α radiation ($\lambda = 1.54056 \text{ \AA}$). X-ray photoelectron spectroscopy (XPS, VG Microtech ESCA 2000, UK) measurements of the nanocomposites were conducted using Perkin-Elmer PHI system with a monochromatic Al K α radiation ($h\nu = 1486.6 \text{ eV}$) as an X-ray source. The optical properties of the as-synthesized samples were also investigated by UV–Vis spectrophotometer (Agilent-8453, Germany) in the wavelength range of 300–800 nm. Photoluminescence (PL) spectra of the nanocomposites were recorded in the range of 350–600 nm at room temperature using the excitation wavelength of 325 nm. Besides, Fourier transform infrared (FTIR) analyses were obtained by an FT-IR spectrometer.

2.3 Photocatalytic Activity

The photocatalytic performance of the as-prepared AZO–RGO nanocomposites was evaluated through the photo-degradation of methyl orange (MO) as a typical water pollutant upon the absorption spectroscopy. At first, 40 mg of photo-catalyst was added to 40 ml of aqueous MO solution (25 mg/l) by stirring. Then, this process was repeated for all the samples to prepare solutions with different catalysts. The obtained solutions were stirred in a dark place at 25 °C for 30 min to reach the adsorption–desorption equilibrium between the catalyst and MO dye. In order to start the photocatalytic reaction, each solution was exposed to visible light using a metal lamp (30 W, G30T8-Philips, $\lambda_{\text{max}} = 460 \text{ nm}$) as a radiation source. Under light irradiation, 4 ml of the solution was taken out at certain time intervals (30, 60, 120, and 180 min), centrifuged to remove the catalyst and then recorded its UV–Vis spectrum. As a control experiment, photocatalytic activity of MO solution and pure ZnO was also evaluated under the same conditions in the absence of the catalyst.

3 Results and Discussion

3.1 Structural Investigations

SEM images were obtained to study the surface morphology of GO layers and consider the loading content of the AZO nanoparticles (AZO NPs) on the RGO surface. A typical SEM image (Fig. 1a) showed that the GO layers have been successfully synthesized. The image shows that these layers not only have distinct edges but also consist the wrinkles on their surface with a few micrometers in length. AFM analysis, which was carried out to investigate the thickness of a typical GO layer, shows that the thickness of this layer is about 1.63 nm (<5 layers) [29]. As can be observed in the SEM image of AZO–RGO nanocomposite (Fig. 1c), AZO NPs have almost uniformly distributed on the GO surfaces and formed AZO–RGO nanocomposites.

TEM image was utilized to analyze the microstructure of prepared AZO–RGO nanocomposite, (Fig. 1d). As can be seen in Fig. 1d, GO sheet has a 2D structure with some clear wrinkles on its surface. Moreover, AZO NPs (most of which smaller than 50 nm in diameter) have randomly anchored on the surface of RGO. Moreover, Fig. 1d exhibits that the presence of RGO sheet into the nanocomposite can provide a hard frame to limit the growth and agglomeration processes of AZO NPs on RGO surface [28]. EDX spectrum of the as-prepared nanocomposite demonstrates the existence of Zn, O, C, and Al elements into the nanocomposite (Fig. 1e), confirming the successful preparation of AZO–RGO nanocomposite [22].

3.2 BET Specific Surface Area Measurements

Since the specific surface area of materials has a crucial role in their photocatalytic activity, the BET measurements of ZnO–RGO and AZO–RGO nanocomposites were achieved and summarized in Table 1. The obtained BET results revealed that the decoration of GO by ZnO and AZO nanoparticles can gradually increase the specific surface area of the nanocomposites by increasing Al content and provide larger active sites on the surface for enhancing the photocatalytic activity [64, 66]. A similar behavior has been reported in the previous studies [41, 50].

3.3 XRD Analysis

Figure 2a presents the XRD patterns of the prepared graphene oxide (GO) and reduced graphene oxide (RGO). It can be seen in this figure that GO has a high-intensity peak at $2\theta = 11.36^\circ$, attributing to the (002) plane. By reduction of GO into RGO, this peak vanished and a low-intensity broad peak appeared at $2\theta = 25^\circ$, assigning to the disordered stacking of RGO into the nanocomposite [72]. This shift is related to the decrease in functional groups on the surface of GO during the reduction treatment.

Figure 2b indicates the XRD patterns of pure ZnO NPs, ZnO–RGO and AZO–RGO nanocomposites with different Al concentrations. It can be seen in this figure that all of the peaks have similar diffraction patterns, corresponding to the hexagonal wurtzite structure of ZnO (JCPDS card, No. 36-1451). Moreover, there are no additional diffraction peaks in the XRD analyses of the samples, assigning to the secondary phases or other compositions such as ZnAl_2O_4 . Therefore, Al dopants can be doped into ZnO lattice for generating the AZO NPs [33]. It was recognized that the electrostatic force between Zn^{2+} ions and the oxygen-containing functional groups on GO sheet could play a significant role for depositing AZO NPs on the surface of GO and then the formation of steady AZO–RGO nanocomposites [47].

3.4 XPS Spectral Characterization

XPS analysis was employed to investigate the surface chemical bonds and binding energies of the synthesized AZO–RGO nanocomposites. Figure 3a exhibits a survey XPS spectrum of 5% AZO–RGO nanocomposite and the characteristic peaks of C1s (284.8 eV), O1s (532 eV), and Zn2p (1046 and 1022.9 eV), confirming the presence of Zn atoms in the as-synthesized sample.

Figure 3b illustrates the high-resolution XPS spectrum of Zn2p. In this figure, two peaks are noticed at 1022.9 eV and 1046 eV binding energies attributing to the Zn-2p_{3/2} and Zn-2p_{1/2}, respectively, which confirm the presence of ZnO NPs with the wurtzite phase in the nanocomposites [44]. The

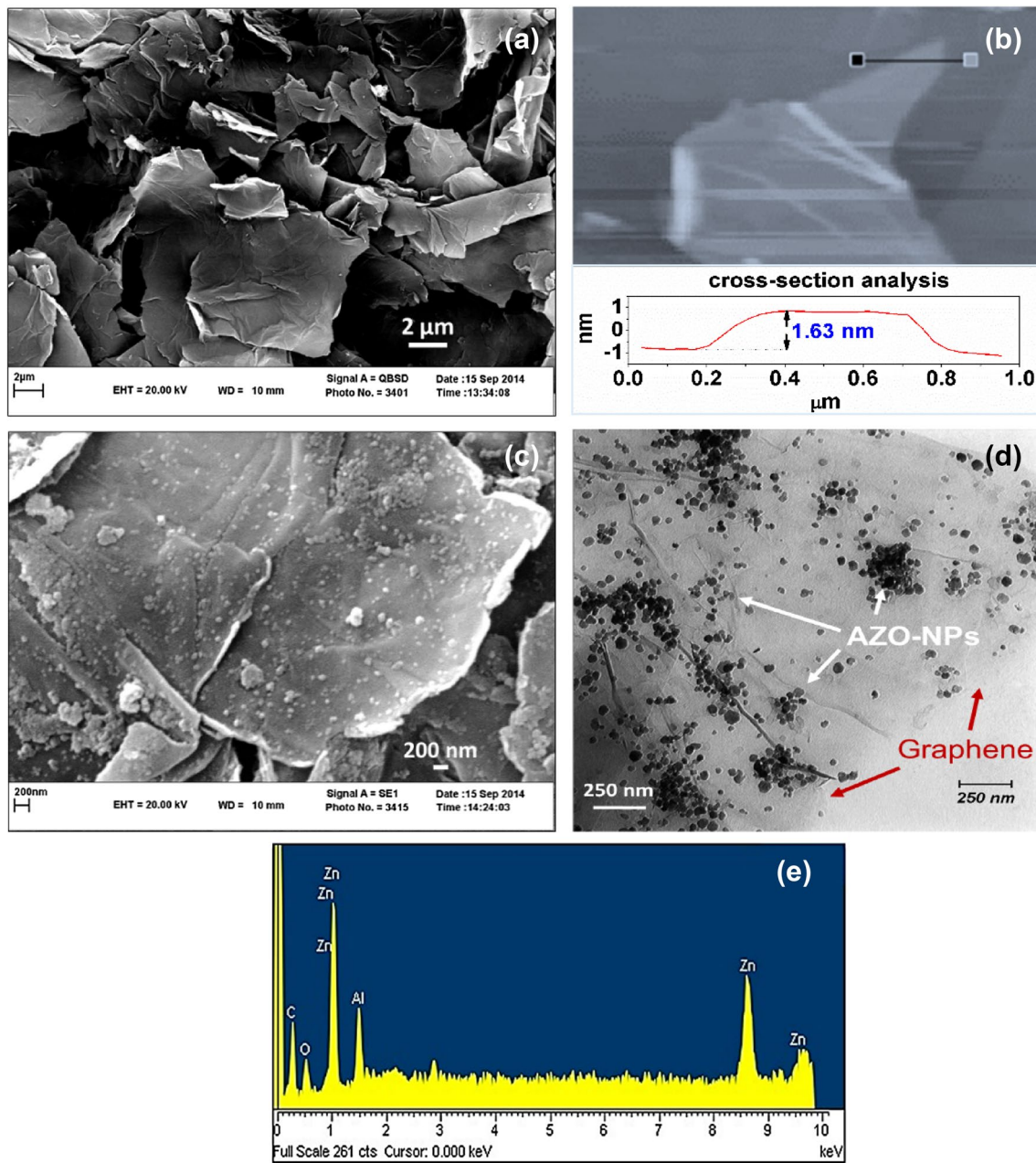


Fig. 1 SEM image of **a** GO sheets, **b** a typical AFM image of the graphene oxide sheet, **c** SEM image, **d** TEM image and **e** EDX spectrum of 5% AZO–RGO nanocomposite

Table 1 Specific surface area of AZO–RGO nanocomposites

Al concentration (wt%)	Surface area (m ² /g)
0	14.72
1	20.39
3	24.87
5	27.43

CasaXPS software with a linear baseline and Gaussian function was employed to peak-fit the high-resolution C1s peak of 5% AZO–RGO sample (Fig. 3c). To correct XPS spectrum of the sample, the C–C component of carbon is commonly used as a set. This value for the high concentration of sp² carbon (such as graphene) is 285 eV. The peak-fitted peaks located at the binding energies of 284.8 eV, 285.9 eV, and 288.6 eV are indexed to C–C (or C=C), C–O, and O–C=O bonds, respectively [35, 62]. As reported in the literature, there are four peaks at 284.6 eV, 286.7 eV, 287.5 eV, and 288.3 eV binding

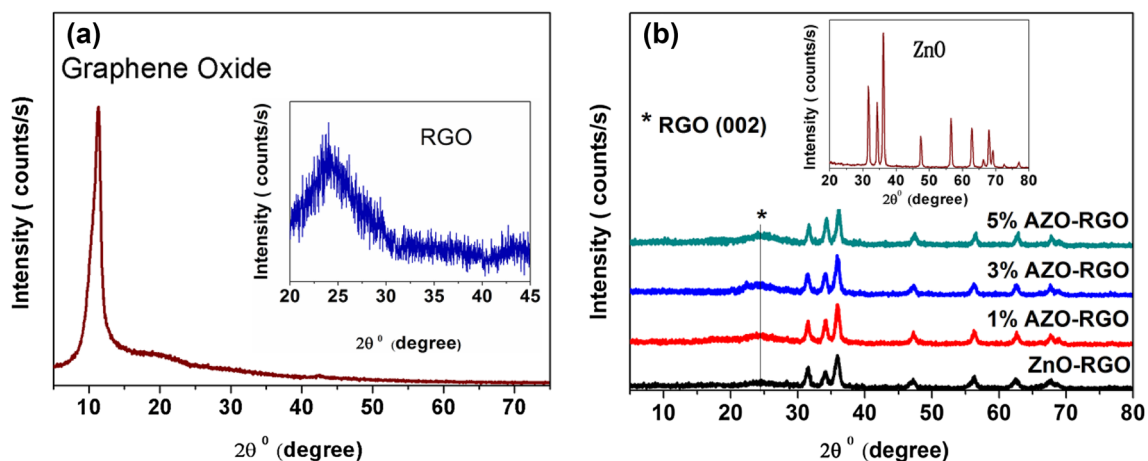


Fig. 2 XRD patterns of **a** graphene oxide (GO) and reduced graphene oxide (RGO), **b** pure ZnO and AZO-RGO nanocomposites with 1%, 3%, and 5% Al concentrations

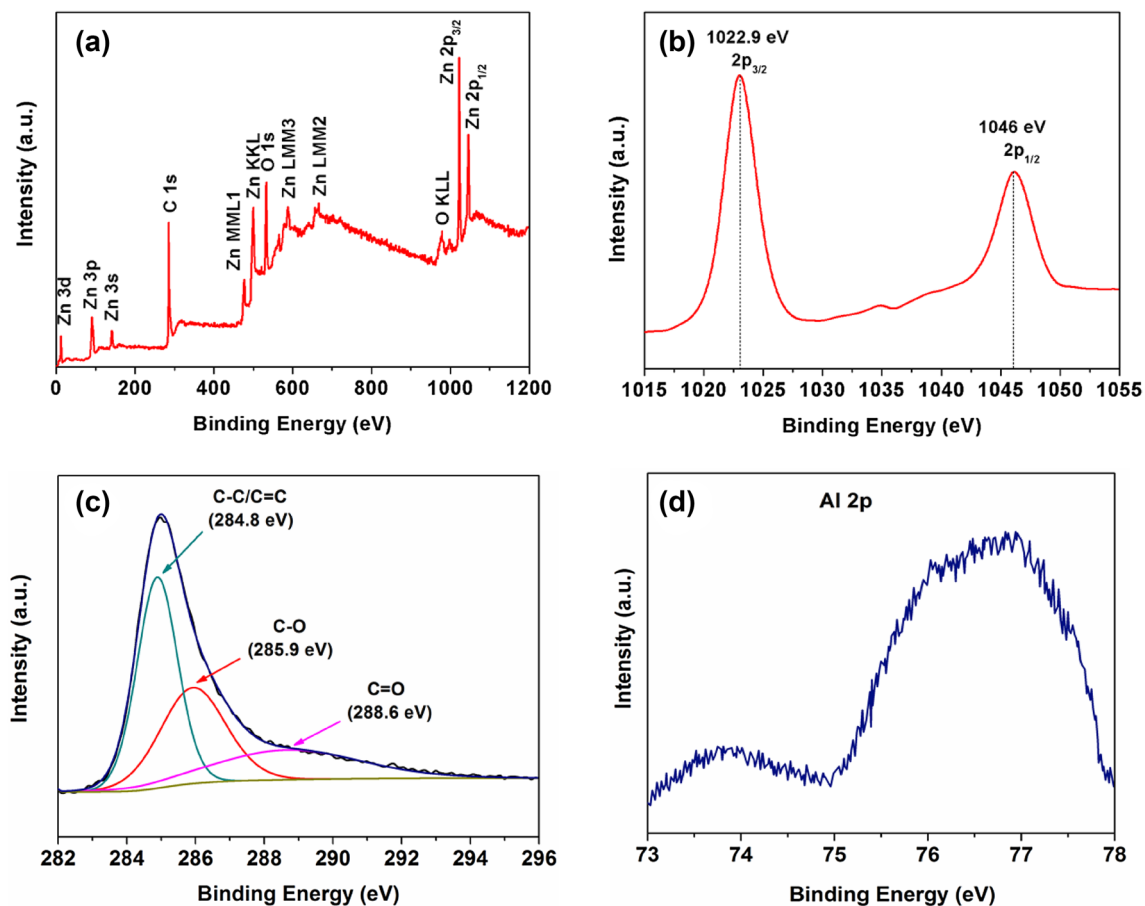


Fig. 3 **a** Survey XPS spectrum, **b** high resolution spectrum of Zn2p region, **c** peak-fitted XPS spectra of C1s and **d** magnified Al2p region for 5% AZO-RGO nanocomposite

energies in the peak-fitted XPS spectrum of GO [17]. Among these values, the binding energies of 286.7 eV, 287.5 eV, and 288.3 eV are attributed to the oxygen-containing groups

on the surface of GO [66]. The decoration of GO sheets by AZO NPs can dramatically decrease the intensity of these peaks, resulting in the reduction of GO into RGO during the

preparation process (Fig. 3c). Due to exist the low content of Al dopant in ZnO lattice, Al peaks cannot appear in the XPS survey spectrum of the nanocomposite (Fig. 3a). To observe the characteristic peaks of Al2p, the binding energy region among 73–78 eV was magnified (Fig. 3d). The peaks located at 73.9 eV and 76.4 eV binding energies are assigned to Al–O and Al–OH bonds, respectively. As shown in this figure, the binding energy of the first peak (73.9 eV) is higher than that of elemental Al (72.7 eV) but is lower than that of Al–OH (76.4 eV), attributing to the low level of Al in ZnO lattice. A similar behavior has been reported previously [24, 36].

3.5 Optical Characterization

UV–Vis absorption analysis was used to study the optical properties of the prepared AZO–RGO nanocomposites. The UV–Vis absorption spectra of the ZnO–RGO and AZO–RGO nanocomposites were obtained (Fig. 4a). As reported in the literature, pure ZnO is able to absorb UV light intensively with its absorption edge placed at about 400 nm [38]. As shown in Fig. 4a, the incorporation of GO in the nanocomposites can increase their visible light absorption. Besides, by increasing Al content in the nanocomposites, the absorption edges of the AZO–RGO nanocomposites present a negligible red-shift. To observe the red-shift, towards higher wavelength, the extrapolation of liner portion of the $(\alpha h\nu)^2$ versus the photon energy ($h\nu$) was done for the nanocomposites (Fig. 4a). This red-shift can describe the exchange interactions between the outer-shell electron of Al ($3p^1$), ‘s’, and ‘p’ electrons of ZnO and/or large scattering effects [30]. In order to calculate the optical band gap of un-doped and Al-doped ZnO NPs–RGO nanocomposites, the Tauc relationship was used [37].

$$(\alpha h\nu)^2 = A(h\nu - E_g)$$

where α , $h\nu$, and A are the optical absorption coefficient, the photon energy, and the constant of proportionality, respectively. E_g is the direct energy band gap of ZnO. Here, the absorption coefficient (α) was calculated, from the raw absorbance data, using the following equation:[50]

$$\alpha = 2.303 \frac{B}{d(\text{cm})}$$

where B is the measured absorbance and d is the thickness of UV–Vis cell ($d=1$ cm). As can be seen in Fig. 4a, a decrease in absorbance occurs at a higher wavelength (around 360 nm), which can be attributed to the energy band gap of ZnO. The energy band gaps of the ZnO–RGO and AZO–RGO nanocomposites were calculated using the obtained UV–Vis spectra. For ZnO–RGO sample, E_g was calculated to be about 3.37 eV, while this value for various AZO–RGO nanocomposites (1%, 3%, and 5% Al concentrations) was 3.35 eV, 3.37 eV, and 3.38 eV, respectively. These values indicate that the calculated energy band gaps for the as-prepared samples are larger than those of pure ZnO (3.32 eV). It is well known that, the substitution of Al^{3+} instead of Zn^{2+} in the ZnO structure can generate free electrons in the conduction band due to the Burstein–Moss effect [63]. Therefore, the energy band gaps of the nanocomposites can increase in comparison with pure ZnO by increasing the Al concentration in the samples [46].

3.6 Photoluminescence (PL) Analysis

The separation and recombination processes of the photo-generated electrons and holes can be studied by PL measurements. Figure 4b exhibits the PL spectra of pure ZnO and AZO–RGO nanocomposites acquired at an excitation wavelength of 325 nm. As can be seen, the PL spectrum of ZnO has two emission peaks within the ultraviolet and

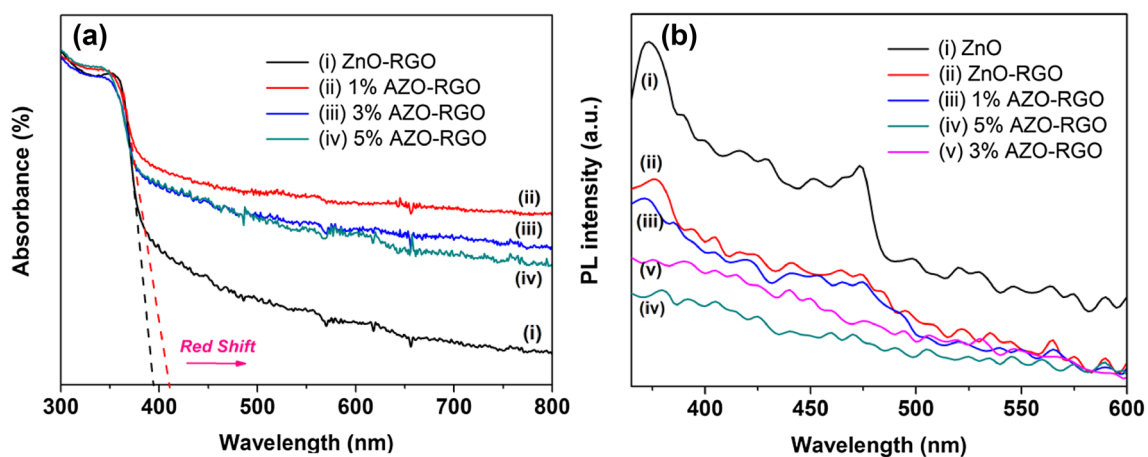


Fig. 4 **a** UV–Vis absorption spectra of ZnO–RGO and AZO–RGO nanocomposites and **b** room-temperature PL emission spectra of ZnO and the prepared nanocomposites with different percent of Al

visible light ranges. These peaks correspond to the recombination of the near band gap (NBE) free excitons and the structural defects, respectively [15, 27, 57]. It is known that, these peaks are dependent on various factors such as particle size, shape, and temperature and preparation method [27]. Moreover, Fig. 4b shows the broad peak detected within the range 450–500 nm, corresponding to the pure ZnO, almost vanished in the PL spectra of AZO–RGO samples. This peak implies several defect states such as oxygen and zinc vacancies, oxygen interstitials, zinc interstitials and oxygen anti-sites in ZnO [1, 12]. Doping ZnO with Al atoms can reduce these sites due to the occupation of intrinsic defect sites by dopants. As shown in Fig. 4b, the intensity of defect peak is drastically reduced, confirming the decrease in defect sites [7]. These results suggest the recombination process, which plays an important role in the photocatalytic efficiency, has been approximately suppressed in the as-prepared AZO–RGO nanocomposites by increasing of Al concentration.

3.7 FT-IR Analysis

FTIR analysis was carried out to study the molecular structure of pure ZnO and the as-prepared GO, ZnO–RGO, and AZO–RGO nanocomposites (Fig. 5). Figure 5a shows an absorption peak at 460 cm^{-1} , ascribing to the stretching vibration between Zn and O atoms [18]. In FTIR spectrum of GO (Fig. 5b), the characteristic absorption bands of the oxide groups are located at 3445 cm^{-1} (O–H, hydroxyl and carboxylic stretching vibration bonds), 1732 cm^{-1} (C=O stretching vibration bond), 1615 cm^{-1} (C=C, C=O Quinone and carboxylate bonds), 1221 cm^{-1} (C–O epoxy stretching bond), and 1050 cm^{-1} (C–O alkoxy stretching bond) [2]. The presence of oxygen-containing groups on the GO surface can possibly increase the covalent bonds between AZO NPs and GO surface. Therefore, these functional groups are the

major factors for creating AZO–RGO nanocomposite [20, 34, 70]. Besides, Fig. 5b shows the bands at 1732 cm^{-1} and 1050 cm^{-1} have been decreased considerably or disappeared entirely after loading ZnO and AZO NPs on the GO surface, implying the elimination of most functional groups on the surface [56]. These results further confirm the reduction of GO into RGO during the solvothermal treatment.

Moreover, two absorption bands appeared in the FTIR spectra of ZnO–RGO and AZO–RGO nanocomposites at 460 cm^{-1} (Fig. 5b). These bands are attributed to the stretching vibration of Zn–O bond and exhibited good agreement with Fig. 5a. There is a weak absorption peak at 500 cm^{-1} in the FTIR spectrum of ZnO–RGO (Fig. 5b), indexed to the oxygen vacancies in ZnO lattice. This peak vanished in the FTIR spectrum of AZO–RGO. It can confirm the reduction of the oxygen vacancies in the nanocomposite by the presence of Al dopants [3, 8, 63]. The low-intensity peak at around 683 cm^{-1} in the FTIR spectrum of AZO–RGO corresponds to the Al–O stretching mode [3].

3.8 Assessment of Photocatalytic Activity

Since carbonaceous materials such as GO have a high potential for adsorbing aromatic pollutants, the synthesized AZO–RGO nanocomposites are expected to be able to adsorb organic pollutants in aqueous solutions. Hereupon, the photocatalytic activity of the nanocomposites was considered for removing the methyl orange (MO) dye from water (Fig. 6). MO dye is generally used as a typical water pollutant for the photocatalytic assessment of materials due to its alkaline and non-biodegradable features [23]. In this study, the photocatalytic activity of the as-synthesized nanocomposites was carried out by monitoring MO discoloration in an aqueous solution. Figure 6a exhibits a profile of the photocatalytic degradation of MO using pure ZnO, ZnO–RGO, and AZO–RGO nanocomposites

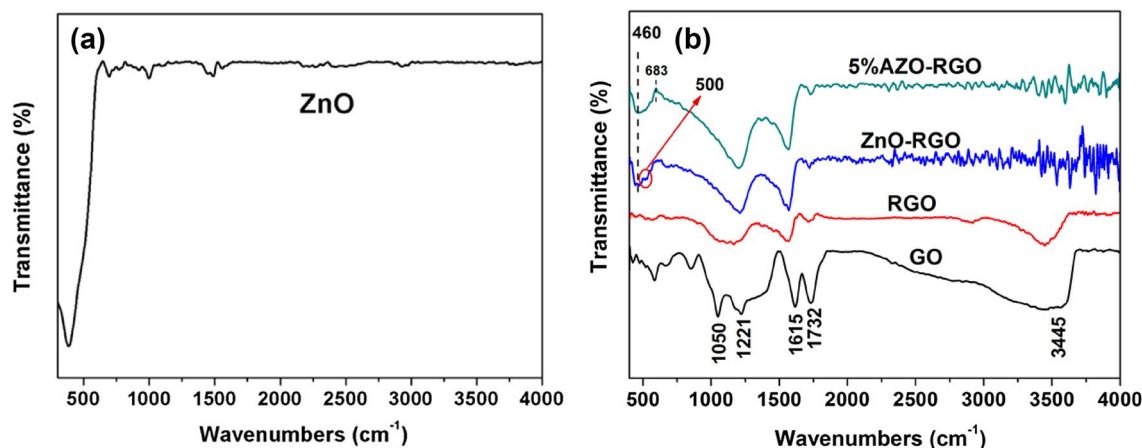


Fig. 5 FT-IR spectra of a pure ZnO and b GO, RGO, ZnO–RGO, and 5% AZO–RGO

under visible light irradiation. In this figure, Y-axis shows the normalized temporal concentration changes (C/C_0) of MO in which C_0 and C are the initial and actual MO concentrations at different irradiation times, respectively. This ratio is proportional to the absorbance ratio (A/A_0), which is derived from the changes in MO absorption profile [71]. As shown in Fig. 6a, in the absence of a catalyst, the degradation of MO is almost negligible even after exposure to 3 h, suggesting that MO dye is stable completely under visible light irradiation [53]. Figure 6a also shows the decrease of MO concentration in the ZnO–RGO and AZO–RGO samples is more than that of pure ZnO under the same conditions, suggesting the synergetic effects of graphene oxide and Al dopants on their photo-catalysis. Therefore, the decoration of GO by ZnO NPs can increase the specific surface area of the sample to adsorb more MO molecules on its surface. In addition, some Al dopants can reside on ZnO boundary as the anchoring sites for adsorbing further dye molecules [1, 25, 54]. However, Fig. 6a–vi indicates that the photocatalytic activity of the sample was decreased by increasing of doping level-up to 10 wt%. This result suggests that the higher dopant concentration may provide additional centers to recombine the photo-induced electron–hole pairs, resulting in the decrease of photocatalytic efficiency of the samples. In this study, however, 5% Al concentration was obtained as an optimal value for doping ZnO. Besides, the measured photocatalytic results show that 5% AZO–RGO nanocomposite is able to degrade MO dye with maximum efficiency at about 80% in 60 min. The absorption spectrum of the original MO solution and its time-dependent absorption spectra are presented in Fig. 6b for 5% AZO–RGO sample during light irradiation. This figure shows the MO absorption

peak intensity has decreased significantly by increasing the exposure time, indicating the degradation of MO dye continuously by the catalyst.

The pseudo-first-order reaction kinetics are normally used to calculate the photocatalytic degradation of organic dyes at low concentrations [42].

$$\ln(C_0/C) = k_{app}t$$

where k_{app} is the apparent reaction rate constant, which is the most important parameter to compare the photocatalytic performance of materials. A linear fitting of $\ln(C_0/C)$ versus irradiation time was carried out to calculate the k_{app} of the as-prepared photo-catalysts (Fig. 7).

The computed k_{app} values were 0.00115, 0.00278, and 0.01001 min^{-1} for pure ZnO, ZnO–RGO, and 5% AZO–RGO, respectively. According to the obtained results, 5% AZO–RGO nanocomposite has the highest reaction constant in comparing to the other catalysts, in which this value is about 8 and 3 times greater than that of ZnO and ZnO–RGO, respectively. This result reveals that the slight introduction of Al dopant (i.e. 5 wt%) can enhance the photocatalytic activity of the sample, probably due to the morphology of the photo-catalyst. The specific surface area of catalyst has been identified to play an important role on its photo-catalysis [10]. As shown in the present work, the specific surface area of the prepared nanocomposites was increased by increasing of Al content (Table 1). This result can confirm the higher adsorption of MO molecules onto the photo-catalyst and also the generation of active sites, resulting in the higher photocatalytic activity of AZO–RGO nanocomposites compared to the pure ZnO.

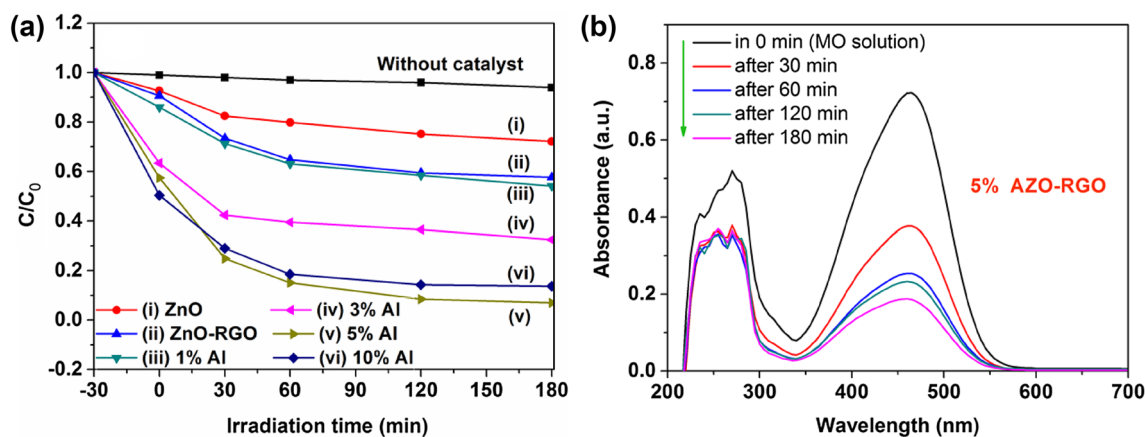


Fig. 6 **a** The photocatalytic decoloration of MO by *i* ZnO, *ii* ZnO–RGO, *iii* 1% AZO–RGO, *iv* 3% AZO–RGO, *v* 5% AZO–RGO, and *vi* 10% AZO–RGO nanocomposites under light irradiation and **b** time

dependent absorption spectra of MO aqueous solution under visible light irradiation in the presence of 5% AZO–RGO nanocomposite

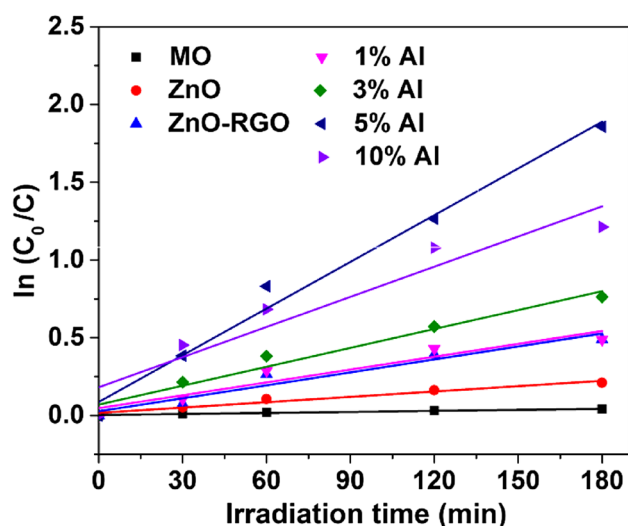


Fig. 7 Plots of $\ln(C_0/C)$ versus time for ZnO, ZnO-RGO, and AZO-RGO catalysts with different Al concentrations (1, 3, 5, and 10 wt%)

3.9 Evaluation of Oxygen Content on the Photo-catalysis

When a semiconductor catalyst is excited by light, its valence band electrons can transfer to the conduction band and create holes in its valence band. Hence, the existence of catalyst in an aquatic system can not only make the extraction of hydroxide ions from water but also react the ions with its holes to making hydroxyl radicals ($\bullet\text{OH}$). Therefore, these active radicals are main factors in the photo-catalysis for decomposing organic molecules [26]. In addition, oxygen molecules can also capture the photo-generated electrons to create super oxide ions ($\bullet\text{O}_2^-$), resulting in the extra generation of hydroxyl radicals. This result suggests that the photocatalytic activity of a catalyst can be enhanced by increasing of oxygen molecules. In order to investigate this effect, the photocatalytic activity of the as-prepared 5% AZO-RGO nanocomposite was accomplished in the bubbling and non-bubbling oxygen conditions (Fig. 8).

The k_{app} values for 5% AZO-RGO were calculated to be 0.03048 and 0.02034 min^{-1} in the bubbling and non-bubbling oxygen conditions, respectively. It can be seen in this figure, the k_{app} coefficient is almost the same for two situations in the first 30 min. It indicates the dissolved oxygen in the solution is nearly adequate to promote the photocatalytic performance of the sample. Therefore, the photocatalytic efficiency of the sample can be improved by bubbling oxygen condition.

3.10 Photo-catalysis Mechanism

As reported previously, the fast recombination process between photoelectron and hole pairs is the greatest issue

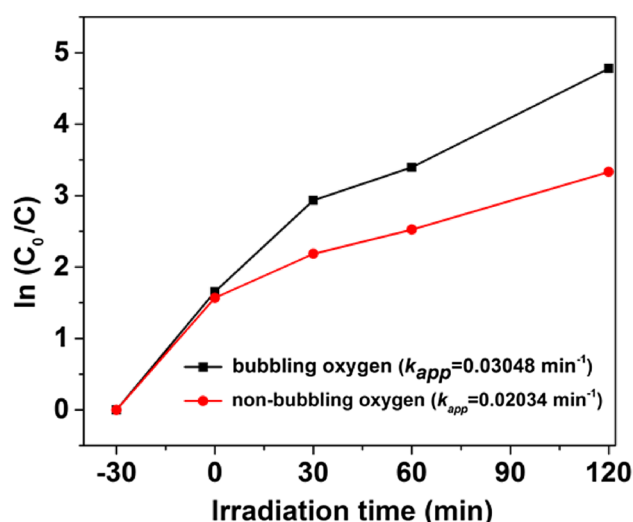
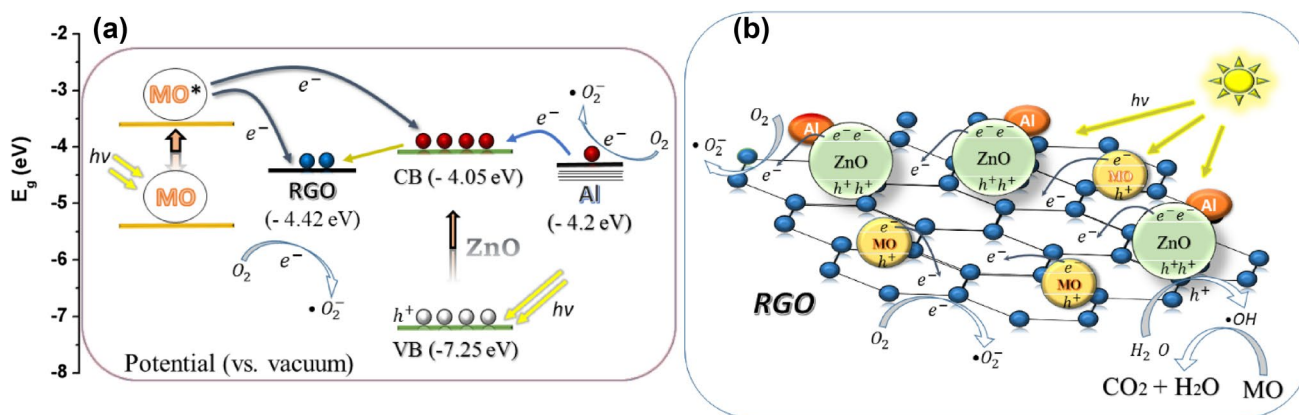


Fig. 8 The effect of oxygen on the photocatalytic activity of 5% AZO-RGO nanocomposite

for enhancing the photocatalytic activity of ZnO. One of the conventional methods for suppressing this process is doping ZnO with different dopants, which has been reported in many studies. Based on the obtained results, the enhanced photocatalytic activity of AZO-RGO nanocomposites compared to the pure ZnO may be related to the synergetic effects of Al dopants and reduced graphene oxide sheets. Therefore, a possible photocatalytic mechanism can be proposed for the AZO-RGO nanocomposite (Scheme 1). As mentioned in literature, the conduction and valence bands of ZnO are located at -4.05 eV and -7.25 eV (vs. vacuum), respectively [39]. Besides, the work functions of reduced graphene oxide and the excited MO are located in -4.5 eV and -3.5 eV , respectively [51]. The energy levels relating to the AZO-RGO catalyst is observed in Scheme 1a. As shown in this figure, the photoelectron and hole pairs can be created during the exposure of the sample by visible light irradiation, resulting in the transferring of the photoelectrons to the conduction band of ZnO. The presence of Al dopants into the ZnO conduction band can also generate extra electrons in the ZnO conduction band. Due to the energy level of the reduced graphene oxide (RGO) is lower than the conduction band of ZnO; therefore, the photo-generated electrons would be able to move on the surface of reduced graphene oxide sheet. Moreover, MO molecules can be excited by light during light irradiation and then the photo-induced electrons may move toward the energy level of the reduced graphene oxide and also ZnO conduction band. Consequently, the electrons transferred on the surface of reduced graphene oxide would react with oxygen molecules for producing the oxygen peroxide radicals ($\bullet\text{O}_2^-$) and hydrogen peroxide (H_2O_2). The hydroxyl radicals ($\bullet\text{OH}$), which



Scheme 1 **a** Energy level diagrams of excited MO, reduced graphene oxide (RGO), ZnO and Al. **b** Simulated mechanism of photo-catalysis in AZO–RGO nanocomposite for organic dye degradation by light

are the main factors for degrading MO dye, can be prepared by reaction of ($\bullet\text{O}_2^-$) and H_2O_2 . In addition, the photo-generated holes can decompose MO molecules either by reacting with hydroxyl ions (OH^-) derived from water or by themselves directly when they are captured by organic compounds on AZO–RGO surface (Scheme 1b). Consequently, the existence of RGO in the nanocomposite not only can prepare the large specific surface area for adsorbing MO molecules but also can supply more reactive oxygen-containing species for degrading organic compounds. Moreover, it may suggest the enhancement of photocatalytic property of the AZO–RGO sample.

4 Conclusions

In summary, AZO–RGO nanocomposites were successfully synthesized by a one-step and low-temperature solvothermal method without any change in the crystalline structure of ZnO. In this study, AZO NPs and RGO nanosheets were obtained synchronously to prepare AZO–RGO nanocomposite. SEM and TEM images demonstrate the formation and rather uniformly distribution of AZO NPs on the RGO surface. Among all the prepared samples, 5% AZO–RGO nanocomposite indicated the highest photocatalytic efficiency for degrading MO molecules of water under visible-light irradiation. This enhanced photocatalytic activity can be related to the presence of RGO sheets and Al dopants into the nanocomposite. Accordingly, reduced graphene oxide nanosheets are able to increase the light absorption and reduce the charge recombination process. These factors are responsible for enhancing the photocatalytic activity of AZO–RGO nanocomposite. Our results finally showed that, AZO–RGO nanocomposites can present new possibilities for promoting the environmental applications of photo-catalysts.

Compliance with Ethical Standards

Conflict of interest The authors declare that they have no conflict of interest.

Informed Consent Informed consent was obtained from all individual participants included in the study.

Research Involving Human Participants and/or Animal This article does not contain any studies with human participants or animals performed by any of the authors.

References

1. M. Ahmad, E. Ahmed, Y. Zhang, N.R. Khalid, J. Xu, M. Ullah, Z. Hong, Preparation of highly efficient Al-doped ZnO photocatalyst by combustion synthesis. *Curr. Appl. Phys.* **13**, 697–704 (2013). <https://doi.org/10.1016/j.cap.2012.11.008>
2. O. Akhavan, R. Azimirad, S. Safa, Functionalized carbon nanotubes in ZnO thin films for photoactivation of bacteria. *Mater. Chem. Phys.* **130**, 598–602 (2011). <https://doi.org/10.1016/j.matchemphys.2011.07.030>
3. S.S. Alias, A.B. Ismail, A.A. Mohamad, Effect of pH on ZnO nanoparticle properties synthesized by sol–gel centrifugation. *J. Alloy. Compd.* **499**, 231–237 (2010). <https://doi.org/10.1016/j.jallcom.2010.03.174>
4. F.A. Alshamsi, A.S. Albadwawi, M.M. Alnuaimi, M.A. Rauf, S.S. Ashraf, Comparative efficiencies of the degradation of Crystal Violet using UV/hydrogen peroxide and Fenton's reagent. *Dyes Pigm.* **74**, 283–287 (2007). <https://doi.org/10.1016/j.dyepig.2006.02.016>
5. S. Ameen, H.-K. Seo, M. Shaheer Akhtar, H.S. Shin, Novel graphene/polyaniline nanocomposites and its photocatalytic activity toward the degradation of rose Bengal dye. *Chem. Eng. J.* **210**, 220–228 (2012). <https://doi.org/10.1016/j.cej.2012.08.035>
6. S. Ameen, M.S. Akhtar, H.-K. Seo, H.S. Shin, Advanced ZnO–graphene oxide nanohybrid and its photocatalytic. *Appl. Mater. Lett.* **100**, 261–265 (2013). <https://doi.org/10.1016/j.matlet.2013.03.012>
7. R. Beura, P. Thangadurai, Structural, optical and photocatalytic properties of graphene–ZnO nanocomposites for varied

- compositions. *J. Phys. Chem. Solids* **102**, 168–177 (2017). <https://doi.org/10.1016/j.jpcs.2016.11.024>
8. I.Y.Y. Bu, Highly conductive and transparent reduced graphene oxide/aluminium doped zinc oxide nanocomposite for the next generation solar cell. *Appl. Opt. Mater.* **36**, 299–303 (2013). <https://doi.org/10.1016/j.optmat.2013.09.012>
 9. Y. Bu, Z. Chen, W. Li, B. Hou, Highly efficient photocatalytic performance of graphene–ZnO quasi-shell–core composite material. *ACS Appl. Mater. Interfaces* **5**, 12361–12368 (2013). <https://doi.org/10.1021/am403149g>
 10. D. Chen et al., Graphene-wrapped ZnO nanospheres as a photocatalyst for high performance photocatalysis. *Thin Solid Films* **574**, 1–9 (2015). <https://doi.org/10.1016/j.tsf.2014.11.051>
 11. A.B. Djuricic, Y.H. Leung, A.M.C. Ng, Strategies for improving the efficiency of semiconductor metal oxide photocatalysis. *Mater. Horiz.* **1**, 400–410 (2014). <https://doi.org/10.1039/C4MH00031E>
 12. S. Gayathri, P. Jayabal, M. Kottaisamy, V. Ramakrishnan, Synthesis of ZnO decorated graphene nanocomposite for enhanced photocatalytic properties. *J. Appl. Phys.* **115**, 173504 (2014). <https://doi.org/10.1063/1.4874877>
 13. R. Georgekutty, M.K. Seery, S.C. Pillai, A highly efficient Ag–ZnO photocatalyst: synthesis, properties, and mechanism. *J. Phys. Chem. C* **112**, 13563–13570 (2008). <https://doi.org/10.1021/jp802729a>
 14. O. Gezici, M. Küçükosmanoğlu, A. Ayar, The adsorption behavior of crystal violet in functionalized sporopollenin-mediated column arrangements. *J. Colloid Interface Sci.* **304**, 307–316 (2006). <https://doi.org/10.1016/j.jcis.2006.09.048>
 15. Y. Gong, T. Andelman, G. Neumark, S. O'Brien, I. Kuskovsky, Origin of defect-related green emission from ZnO nanoparticles: effect of surface modification. *Nanoscale Res. Lett.* **2**, 297–302 (2007)
 16. G. Gu, J. Cheng, X. Li, W. Ni, Q. Guan, G. Qu, B. Wang, Facile synthesis of graphene supported ultralong TiO₂ nanofibers from the commercial titania for high performance lithium-ion batteries. *J. Mater. Chem. A* **3**, 6642–6648 (2015). <https://doi.org/10.1039/C5TA00523J>
 17. H.-L. Guo, P. Su, X. Kang, S.-K. Ning, Synthesis and characterization of nitrogen-doped graphene hydrogels by hydrothermal route with urea as reducing-doping agents. *J. Mater. Chem. A* **1**, 2248–2255 (2013). <https://doi.org/10.1039/C2TA00887D>
 18. J. He, C. Niu, C. Yang, J. Wang, X. Su, Reduced graphene oxide anchored with zinc oxide nanoparticles with enhanced photocatalytic activity and gas sensing properties. *RSC Adv.* **4**, 60253–60259 (2014). <https://doi.org/10.1039/C4RA12707B>
 19. N. Herring, S. Almahoudi, C. Olson, M.S. El-Shall, Enhanced photocatalytic activity of ZnO–graphene nanocomposites prepared by microwave synthesis. *J. Nanopart. Res.* **14**, 1–13 (2012). <https://doi.org/10.1007/s11051-012-1277-7>
 20. L. Hu, X. Hu, X. Wu, C. Du, Y. Dai, J. Deng, Density functional calculation of transition metal adatom adsorption on graphene. *Physica B* **405**, 3337–3341 (2010). <https://doi.org/10.1016/j.physb.2010.05.001>
 21. W.S. Hummers, R.E. Offeman, Preparation of graphitic oxide. *Am. Chem. Soc.* **80**, 1339–1339 (1958). <https://doi.org/10.1021/ja01539a017>
 22. M. Isik, N.M. Gasanly, Thermoluminescence properties of Al doped ZnO nanoparticles. *Ceram. Int.* **44**, 13929–13933 (2018). <https://doi.org/10.1016/j.ceramint.2018.04.241>
 23. P. Jantawasu, T. Sreethawong, S. Chavadej, Photocatalytic activity of nanocrystalline mesoporous-assembled TiO₂ photocatalyst for degradation of methyl orange monoazo dye in aqueous wastewater. *Chem. Eng. J.* **155**, 223–233 (2009). <https://doi.org/10.1016/j.cej.2009.07.036>
 24. S.H. Jeong, S. Kho, D. Jung, S.B. Lee, J.H. Boo, Deposition of aluminum-doped zinc oxide films by RF magnetron sputtering and study of their surface characteristics. *Surf. Coat. Technol.* **174–175**, 187–192 (2003). [https://doi.org/10.1016/S0257-8972\(03\)00600-5](https://doi.org/10.1016/S0257-8972(03)00600-5)
 25. S.A. Khayatian, A. Kompany, N. Shahtahmassebi, A.K. Zak, Preparation and characterization of Al doped ZnO NPs/graphene nanocomposites synthesized by a facile one-step solvothermal method. *Ceram. Int.* **42**, 110–115 (2016). <https://doi.org/10.1016/j.ceramint.2015.08.008>
 26. Y.C. Ko, H.Y. Fang, D.H. Chen, Fabrication of Ag/ZnO/reduced graphene oxide nanocomposite for SERS detection and multiway killing of bacteria. *J. Alloy. Compd.* **695**, 1145–1153 (2017). <https://doi.org/10.1016/j.jallcom.2016.10.241>
 27. H.J. Lee, J.H. Kim, S.S. Park, S.S. Hong, G.D. Lee, Degradation kinetics for photocatalytic reaction of methyl orange over Al-doped ZnO nanoparticles. *J. Ind. Eng. Chem.* **25**, 199–206 (2015). <https://doi.org/10.1016/j.jiec.2014.10.035>
 28. X. Li, Q. Wang, Y. Zhao, W. Wu, J. Chen, H. Meng, Green synthesis and photo-catalytic performances for ZnO-reduced graphene oxide nanocomposites. *J. Colloid Interface Sci.* **411**, 69–75 (2013). <https://doi.org/10.1016/j.jcis.2013.08.050>
 29. P. Liu, Y. Huang, L. Wang, A facile synthesis of reduced graphene oxide with Zn powder under acidic condition. *Mater. Lett.* **91**, 125–128 (2013). <https://doi.org/10.1016/j.matlet.2012.09.085>
 30. S. Liu, H. Sun, S. Liu, S. Wang, Graphene facilitated visible light photodegradation of methylene blue over titanium dioxide photocatalysts. *Chem. Eng. J.* **214**, 298–303 (2013). <https://doi.org/10.1016/j.cej.2012.10.058>
 31. X. Liu, J. Zhang, L. Wang, T. Yang, X. Guo, S. Wu, S. Wang, 3D hierarchically porous ZnO structures and their functionalization by Au nanoparticles for gas sensors. *J. Mater. Chem.* **21**, 349–356 (2011). <https://doi.org/10.1039/C0JM01800G>
 32. X. Liu et al., UV-assisted photocatalytic synthesis of ZnO–reduced graphene oxide composites with enhanced photocatalytic activity in reduction of Cr(VI). *Chem. Eng. J.* **183**, 238–243 (2012). <https://doi.org/10.1016/j.cej.2011.12.068>
 33. M. Louhichi, S. Romdhane, A. Fkiri, L.S. Smiri, H. Bouchriha, Structural and photoluminescence properties of Al-doped zinc oxide nanoparticles synthesized in polyol. *Appl. Surf. Sci.* **356**, 998–1004 (2015). <https://doi.org/10.1016/j.apsusc.2015.08.202>
 34. Q.-P. Luo, X.-Y. Yu, B.-X. Lei, H.-Y. Chen, D.-B. Kuang, C.-Y. Su, Reduced graphene oxide-hierarchical ZnO hollow sphere composites with enhanced photocurrent and photocatalytic activity. *J. Phys. Chem. C* **116**, 8111–8117 (2012). <https://doi.org/10.1021/jp2113329>
 35. R. Lv et al., Facile synthesis of ZnO nanorods grown on graphene sheets and its enhanced photocatalytic efficiency. *J. Chem. Technol. Biotechnol.* **90**, 550–558 (2015). <https://doi.org/10.1002/jctb.4347>
 36. N. Neves, A. Lagoa, J. Calado, A.M.B. do Rego, E. Fortunato, R. Martins, I. Ferreira, Al-doped ZnO nanostructured powders by emulsion detonation synthesis—Improving materials for high quality sputtering targets manufacturing. *J. Eur. Ceram. Soc.* **34**, 2325–2338 (2014). <https://doi.org/10.1016/j.jeurceramsoc.2014.02.019>
 37. A.A. Ogwu, E. Bouquerel, O. Ademosu, S. Moh, E. Crossan, F. Placido, The influence of rf power and oxygen flow rate during deposition on the optical transmittance of copper oxide thin films prepared by reactive magnetron sputtering. *J. Phys. D* **38**, 266 (2005)
 38. Y. Peng, J. Ji, D. Chen, Ultrasound assisted synthesis of ZnO/reduced graphene oxide composites with enhanced photocatalytic activity and anti-photocorrosion. *Appl. Surf. Sci.* **356**, 762–768 (2015). <https://doi.org/10.1016/j.apsusc.2015.08.070>
 39. J. Qin, X. Zhang, C. Yang, M. Cao, M. Ma, R. Liu, ZnO microspheres-reduced graphene oxide nanocomposite for photocatalytic

- degradation of methylene blue dye. *Appl. Surf. Sci.* **392**, 196–203 (2017). <https://doi.org/10.1016/j.apsusc.2016.09.043>
40. L.S. Roselin, R. Selvin, Photocatalytic degradation of reactive orange 16 dye in a ZnO coated thin film flow photoreactor. *Sci. Adv. Mater.* **3**, 251–258 (2011). <https://doi.org/10.1166/sam.2011.1151>
 41. P.P. Sahay, R.K. Nath, Al-doped ZnO thin films as methanol sensors. *Sens. Actuators B* **134**, 654–659 (2008). <https://doi.org/10.1016/j.snb.2008.06.006>
 42. B. Saravanakumar, R. Mohan, S.-J. Kim, Facile synthesis of graphene/ZnO nanocomposites by low temperature hydrothermal method. *Mater. Res. Bull.* **48**, 878–883 (2013). <https://doi.org/10.1016/j.materresbull.2012.11.048>
 43. J.-C. Sin, S.-M. Lam, K.-T. Lee, A.R. Mohamed, Preparation and photocatalytic properties of visible light-driven samarium-doped ZnO nanorods. *Ceram. Int.* **39**, 5833–5843 (2013). <https://doi.org/10.1016/j.ceramint.2013.01.004>
 44. R.K. Singhal et al., Room temperature ferromagnetism in Mn-doped dilute ZnO semiconductor: An electronic structure study using X-ray photoemission. *J. Alloy. Compd.* **477**, 379–385 (2009). <https://doi.org/10.1016/j.jallcom.2008.10.005>
 45. Y.M. Slokar, A.M. Le Marechal, Methods of decoloration of textile wastewaters. *Dyes Pigm.* **37**, 335–356 (1998). [https://doi.org/10.1016/S0143-7208\(97\)00075-2](https://doi.org/10.1016/S0143-7208(97)00075-2)
 46. G. Srinet, R. Kumar, V. Sajal, Effects of aluminium doping on structural and photoluminescence properties of ZnO nanoparticles. *Ceram. Int.* **40**, 4025–4031 (2014). <https://doi.org/10.1016/j.ceramint.2013.08.055>
 47. S. Stankovich, R.D. Piner, X. Chen, N. Wu, S.T. Nguyen, R.S. Ruoff, Stable aqueous dispersions of graphitic nanoplatelets via the reduction of exfoliated graphite oxide in the presence of poly(sodium 4-styrenesulfonate). *J. Mater. Chem.* **16**, 155–158 (2006). <https://doi.org/10.1039/B512799H>
 48. V. Subramanian, E.E. Wolf, P.V. Kamat, Green emission to probe photoinduced charging events in ZnO–Au nanoparticles. charge distribution and fermi-level equilibration. *J. Phys. Chem. B* **107**, 7479–7485 (2003). <https://doi.org/10.1021/jp0275037>
 49. H. Sun, S. Wang, H.M. Ang, M.O. Tade, Q. Li, Halogen element modified titanium dioxide for visible light photocatalysis. *Chem. Eng. J.* **162**, 437–447 (2010). <https://doi.org/10.1016/j.cej.2010.05.069>
 50. S. Suwanboon, P. Amornpitoksuk, A. Haidoux, J.C. Tedenac, Structural and optical properties of undoped and aluminium doped zinc oxide nanoparticles via precipitation method at low temperature. *J. Alloy. Compd.* **462**, 335–339 (2008). <https://doi.org/10.1016/j.jallcom.2007.08.048>
 51. L. Sygellou, G. Paterakis, C. Galiotis, D. Tasis, Work function tuning of reduced graphene oxide thin films. *J. Phys. Chem. C* **120**, 281–290 (2016). <https://doi.org/10.1021/acs.jpcc.5b09234>
 52. Tassalit D, Laoufi AN, Bentahar F (2011) Photocatalytic deterioration of tylosin in an aqueous suspension using UV/TiO₂. *Sci. Adv. Mater.* **3**:944–948 <https://doi.org/10.1166/sam.2011.1243>
 53. Y. Tian, B. Chang, J. Fu, F. Xi, X. Dong, Yellow-colored mesoporous pure titania and its high stability in visible light photocatalysis. *Powder Technol.* **245**, 227–232 (2013). <https://doi.org/10.1016/j.powtec.2013.04.036>
 54. K. Ullah, Z.-D. Meng, S. Ye, L. Zhu, W.-C. Oh, Synthesis and characterization of novel PbS–graphene/TiO₂ composite with enhanced photocatalytic activity. *J. Ind. Eng. Chem.* **20**, 1035–1042 (2014). <https://doi.org/10.1016/j.jiec.2013.06.040>
 55. J. Ungelenk, C. Feldmann, Synthesis of faceted [small beta]-SnWO₄ microcrystals with enhanced visible-light photocatalytic properties. *Chem. Commun.* **48**, 7838–7840 (2012). <https://doi.org/10.1039/C2CC33224H>
 56. J. Wang, T. Tsuzuki, B. Tang, X. Hou, L. Sun, X. Wang, Reduced graphene oxide/ZnO composite: reusable adsorbent for pollutant management. *ACS Appl. Mater. Interfaces.* **4**, 3084–3090 (2012). <https://doi.org/10.1021/am300445f>
 57. M. Wang et al., Optical and photoluminescent properties of sol-gel Al-doped ZnO thin films. *Mater. Lett.* **61**, 1118–1121 (2007). <https://doi.org/10.1016/j.matlet.2006.06.065>
 58. B. Weng, J. Wu, N. Zhang, Y.-J. Xu, Observing the role of graphene in boosting the two-electron reduction of oxygen in graphene–WO₃ nanorod photocatalysts. *Langmuir* **30**, 5574–5584 (2014). <https://doi.org/10.1021/la4048566>
 59. P. Worajittiphon, K. Pingmuang, B. Inceesungvorn, N. Wetchakun, S. Phanichphant, Enhancing the photocatalytic activity of ZnO nanoparticles for efficient rhodamine B degradation by functionalised graphene nanoplatelets. *Ceram. Int.* **41**, 1885–1889 (2015). <https://doi.org/10.1016/j.ceramint.2014.09.023>
 60. Q. Xiao, L. Ouyang, Photocatalytic photodegradation of xanthate over Zn_{1-x}MnxO under visible light irradiation. *J. Alloy. Compd.* **479**, L4–L7 (2009). <https://doi.org/10.1016/j.jallcom.2008.12.085>
 61. Q. Xiao, J. Zhang, C. Xiao, X. Tan, Photocatalytic decolorization of methylene blue over Zn_{1-x}CoxO under visible light irradiation. *Mater. Sci. Eng.* **142**, 121–125 (2007). <https://doi.org/10.1016/j.mseb.2007.06.021>
 62. D. Yang et al., Chemical analysis of graphene oxide films after heat and chemical treatments by X-ray photoelectron and Micro-Raman spectroscopy. *Carbon* **47**, 145–152 (2009). <https://doi.org/10.1016/j.carbon.2008.09.045>
 63. N.R. Yogamalar, A.C. Bose, Absorption–emission study of hydrothermally grown Al:ZnO nanostructures. *J. Alloy. Compd.* **509**, 8493–8500 (2011). <https://doi.org/10.1016/j.jallcom.2011.06.012>
 64. J. Yu, J. Jin, B. Cheng, M. Jaroniec, A noble metal-free reduced graphene oxide–CdS nanorod composite for the enhanced visible-light photocatalytic reduction of CO₂ to solar fuel. *J. Mater. Chem. A* **2**, 3407–3416 (2014). <https://doi.org/10.1039/C3TA14493C>
 65. D. Zeng, P. Gong, Y. Chen, C. Wang, D.-L. Peng, Preparation of multi-branched Au–ZnO hybrid nanocrystals on graphene for enhanced photocatalytic performance. *Mater. Lett.* **161**, 379–383 (2015). <https://doi.org/10.1016/j.matlet.2015.08.153>
 66. L. Zhang, N. Li, H. Jiu, G. Qi, Y. Huang, ZnO-reduced graphene oxide nanocomposites as efficient photocatalysts for photocatalytic reduction of CO₂. *Ceram. Int.* **41**, 6256–6262 (2015). <https://doi.org/10.1016/j.ceramint.2015.01.044>
 67. L. Zhang et al., Significantly enhanced photocatalytic activities and charge separation mechanism of Pd-decorated ZnO–graphene oxide nanocomposites. *ACS Appl. Mater. Interfaces* **6**, 3623–3629 (2014). <https://doi.org/10.1021/am405872r>
 68. Y. Zheng, L. Zheng, Y. Zhan, X. Lin, Q. Zheng, K. Wei, Ag/ZnO heterostructure nanocrystals: synthesis, characterization and photocatalysis. *Inorg. Chem.* **46**, 6980–6986 (2007). <https://doi.org/10.1021/ic700688f>
 69. J.B. Zhong, J.Z. Li, X.Y. He, J. Zeng, Y. Lu, W. Hu, K. Lin, Improved photocatalytic performance of Pd-doped ZnO. *Curr. Appl. Phys.* **12**, 998–1001 (2012). <https://doi.org/10.1016/j.cap.2012.01.003>
 70. G. Zhou, D.-W. Wang, L.-C. Yin, N. Li, F. Li, H.-M. Cheng, Oxygen bridges between NiO nanosheets and graphene for improvement of lithium storage. *ACS Nano* **6**, 3214–3223 (2012). <https://doi.org/10.1021/mn300098m>
 71. X. Zhou, T. Shi, H. Zhou, Hydrothermal preparation of ZnO-reduced graphene oxide hybrid with high performance in photocatalytic degradation. *Appl. Surf. Sci.* **258**, 6204–6211 (2012). <https://doi.org/10.1016/j.apsusc.2012.02.131>
 72. F. Zou, Y. Yu, N. Cao, L. Wu, J. Zhi, A novel approach for synthesis of TiO₂–graphene nanocomposites and their photoelectrical properties. *Scr. Mater.* **64**, 621–624 (2011). <https://doi.org/10.1016/j.scriptamat.2010.12.003>